

A combined surface stress and magneto-optical Kerr effect measurement setup for temperatures down to 30 K and in fields of up to 0.7 T

J. Prempfer, D. Sander, and J. Kirschner

Max-Planck-Institut für Mikrostrukturphysik, Weinberg 2, D-06120 Halle/Saale, Germany

(Received 30 April 2012; accepted 24 June 2012; published online 25 July 2012)

An optical 2-beam surface stress measurement and magneto-optical Kerr-effect has been combined with a liquid helium cooled cryostat. Sample temperatures down to 30 K and magnetic fields up to 0.7 T are achieved under UHV conditions. Low temperatures are exploited to obtain the first experimental data on the surface stress change induced by the adsorption of the noble gas Xe on Pt(111). High magnetic fields and low temperatures are used to characterize the magnetic properties of Co monolayers in longitudinal and polar Kerr geometries. The effective magnetic anisotropy is extracted from hard axis magnetization loops. © 2012 American Institute of Physics. [<http://dx.doi.org/10.1063/1.4737384>]

I. INTRODUCTION

Crystal curvature measurements are well established techniques for the determination of film stress and surface stress changes.^{1–17} They have contributed to a quantitative understanding of stress-strain relations in films and characterize adsorbate-induced surface stress changes with sub-monolayer sensitivity. The *in situ* combination of stress-induced crystal curvature measurements with magneto-optical Kerr effect (MOKE) (Ref. 18) measurements offers new insights into the correlation between stress and magnetic anisotropy.¹⁹ Here, the generally observed rapid decrease of the Curie temperature with decreasing film thickness calls for an extension of MOKE measurements to the low temperature range. However, low temperatures may also impede the magnetization reversal process,²⁰ and consequently larger coercivities are often observed with decreasing temperature. Thus, measurements at lower temperatures also call for sizable magnetic fields. Recent approaches already aim at MOKE measurements in large magnetic fields^{21,22} and at low temperatures.²³ Here, we present a combined setup which allows stress and MOKE measurements at low temperature and in large magnetic fields. We use a liquid helium cooled cryostat in conjunction with an electromagnet to perform measurements in the temperature range 30–1300 K and in fields of up to 0.7 T.

Section II provides an overview of the experimental setup. It is followed by a description of the optical 2-beam stress measurement technique. Section III presents the experimental results which illustrate stress and MOKE results at 30 K and in high magnetic fields.

II. EXPERIMENTAL SETUP

A. Cryostat and sample holder

The sample manipulator of the UHV chamber is equipped with a liquid helium cryostat.²⁴ The heat exchange tank of the cryostat is cooled by a continuous flow of liquid helium from a He-dewar vessel to the helium recovery system, as schematically indicated in Fig. 1(a). The consumption

of liquid He is ~ 1.5 l/h at the lowest temperature of 30 K. The sample holder is thermally coupled to the heat exchange tank by a copper braid. Figure 1(b) shows an enlarged view of the sample holder. We use a thin (0.1 mm) cantilever single crystal for the stress measurements.¹⁴ Here, we use a Pt(111) crystal (length = 13 mm, width = 2.5 mm), which is clamped along its width at its top end to the sample manipulator and the bottom end is free, as schematically indicated in Fig. 2. Both crystal surfaces are polished (roughness ≤ 0.03 μm) and crystallographically aligned to $\leq 0.1^\circ$.²⁵ The temperature of the sample holder is measured by two calibrated sensors.

A rhodium-iron-sensor²⁶ measures the temperature below the sample and a Cernox-sensor (zirconium oxy-nitride thin film resistor)²⁶ measures the temperature directly at the heat exchange tank. Both sensors were calibrated against a sensor which was placed onto a dummy crystal, which was mounted in place of the Pt crystal. Both temperature readings are used as a reference for a proportional integral differential-temperature-control-loop. It applies an electrical heating power to the heat exchange tank to adjust temperatures in the range 30–300 K reliably. Higher temperatures of up to 1300 K are accessible by e-beam heating of the crystal from the rear side. This extension of the temperature range from low to high temperatures is an important aspect of this work. It takes 12 min to reach the minimal temperature at the heat exchange tank starting from 300 K. Some 30–45 min later the thermal drift at the sample holder has stabilized, and stress measurements can commence. Comparable time scales apply also to the high temperature range.

It is a challenge to reach temperatures as low as possible at the cantilever sample and to combine this with the possibility of heating the sample for preparation and measurement to temperatures of up to 1300 K. Low temperatures call for an efficient thermal coupling between sample and manipulator, while the wish for moderate heating power for high temperatures favors weak thermal coupling. The chosen layout fulfills these competing requirements.

The sample crystal is heated indirectly from its backside. We place a thermal shield (tungsten foil 0.1 mm) between the e-beam heating filament and the sample crystal, as shown in

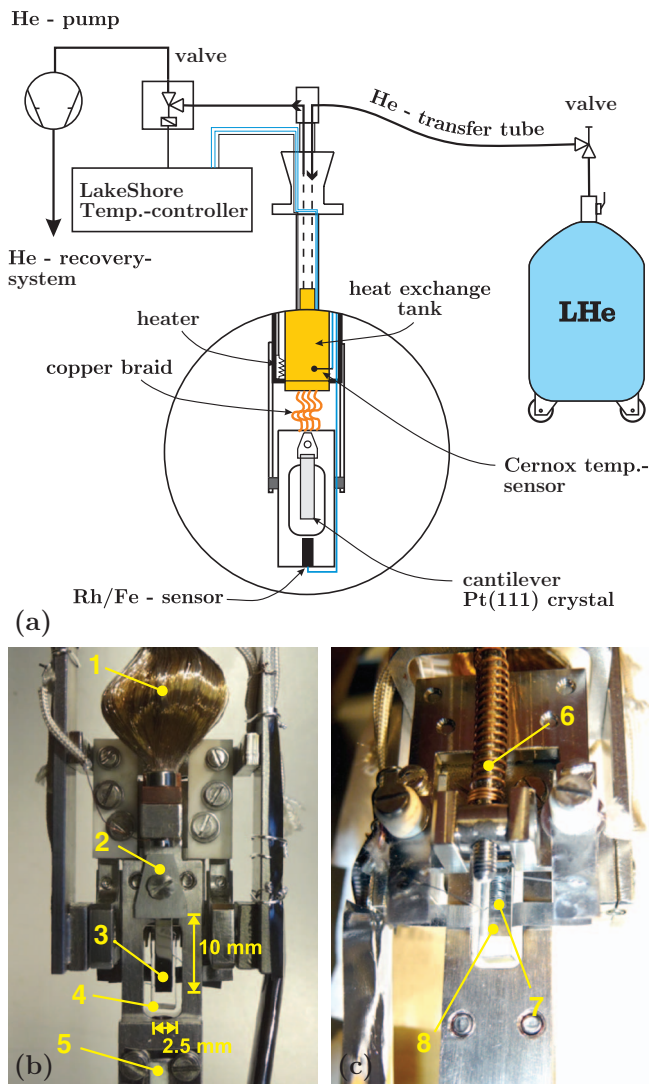


FIG. 1. (a) Scheme of the cryostat system and enlarged schematic view of the sample holder and cantilever crystal, which can be cooled down to 30 K; (b) front view of the sample holder with 1: copper braid, 2: Mo sample clamp, 3: Pt(111) cantilever crystal, 4: Ta shield, 5: fluorescent screen; (c) view from the backside with 6: tilt rod, 7: e-beam filament, 8: W heat shield.

Figs. 1(b) and 1(c). A high voltage (+500 V) with respect to the filament is applied to the tungsten foil to accelerate electrons towards the radiation shield. The rest of the sample holder is screened by a tantalum shield, to minimize unwanted heating of the whole sample holder. This layout ensures that the rather delicate thin cantilever crystal is not damaged by direct e-beam bombardment. Rather, the more uniform radiation of the tungsten foil heats up the crystal.

The temperature of the Pt crystal is checked during heating by an optical pyrometer²⁷ and by an IR pyrometer.²⁸ The comparison of the optical temperature measurements with respective measurements on a dummy crystal with thermocouples indicate an homogeneous (± 5 K) sample temperature over the lower 6 mm near the free end of the crystal. A temperature gradient to lower temperatures is observed near the upper clamping.

A mechanical tilt of the sample holder allows to align the sample normal by $\pm 5^\circ$. It is operated *in situ* by an UHV rota-

tion feedthrough mounted at the top end of the differentially pumped manipulator top flange. This adjustment is mandatory for the alignment of the optical curvature and MOKE measurements and for low energy electron diffraction (LEED) experiments.

B. Surface stress setup

Different experimental setups for the determination of stress are described in the literature.^{1-10,16} We give a short overview of our optical two beam curvature measurement in the following.

Figure 2 shows a schematic view of the setup. The cantilever crystal is clamped at its upper end along its width. Our samples have a large length-to-width ratio (≈ 4), and this minimizes the effect of clamping on the stress-induced curvature. Thus, for a quantitative analysis we can treat the stress-induced curvature as free 2-dimensional bending.¹¹ For a given length-to-width ratio a curvature measurement is preferable in view of an accurate analysis as compared to measurements of stress-induced substrate deflection or stress-induced change of substrate slope.¹¹ Thus, we are confident that the measurement of curvature, as outlined below, gives accurate results for the determination of stress.

The optical 2-beam stress measurement setup^{14,17} is mounted directly on a Conflat(CF)-viewport flange at the UHV chamber. A laser beam²⁹ is split into two beams, and they hit the cantilever crystal at two different positions some millimeters apart along the vertical direction at the lower end of the crystal. The beams are reflected onto two split photodiodes.³⁰ The split-photodiodes serve as position-sensitive detectors.³⁰ The split-photodiodes are connected to an amplifier.³¹ It delivers a difference and a sum signal which indicate the position of the laser beam and the overall illumi-

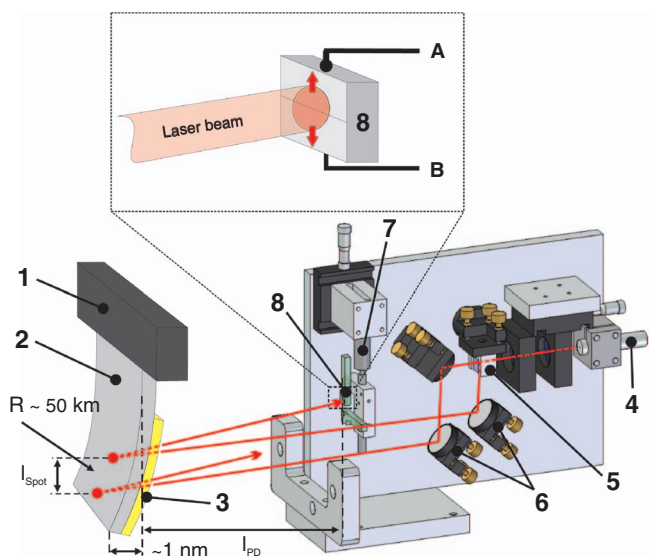


FIG. 2. Scheme of the crystal curvature stress measurement. 1: sample holder, 2: cantilever crystal, 3: adsorbate or film, 4: laser, 5: beam splitter, 6: adjustable mirrors, 7: piezo actuator, 8: split photodetector. The dashed box shows an enlarged view of one of the split photodetectors. The wires A and B of each sensitive area of the diode are connected to an amplifier, which delivers the sum-signal $A + B$ as well as the difference $A - B$.

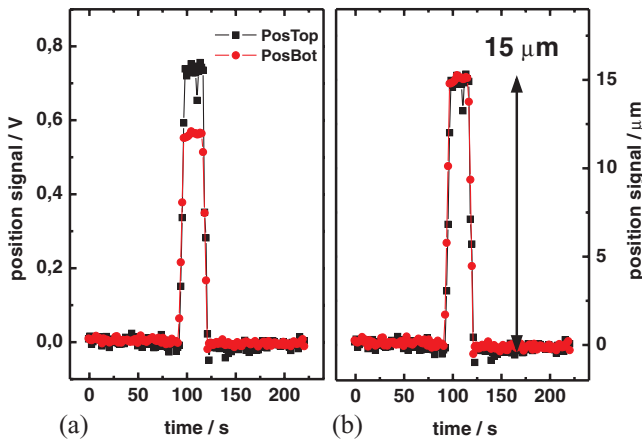


FIG. 3. Calibration measurement to convert the position signal difference ΔU_{Pos} from the upper and lower laser beams into a beam displacement. The detectors are displaced by $15 \mu\text{m}$ by the piezo drive (part 7 in Fig. 2). (a) Raw position voltage signal, (b) position change in μm . The arrow indicates that the signal change corresponds to $15 \mu\text{m}$ displacement of the laser beams on the detectors.

nation of each detector, respectively. A stress-induced change of curvature of the crystal induces a displacement of the reflected beams on the split-photodiodes, and a change of the difference signal results for each detector, whereas the sum signal remains largely unaffected.

The position signals of the split photodetectors are calibrated by the signal change which is induced by a known laser beam displacement. We perform this calibration by moving the split detectors vertically by 0.015 mm by a calibrated piezo drive,³² while the laser beams are stationary. We record the resulting position signal change, as indicated in Fig. 3. Its magnitude differs for both detectors due to slight differences of the beam profiles of both reflected beams. Thus, each detector signal requires a specific calibration factor, which amounts to 0.75 and $0.58 \text{ V}/0.015 \text{ mm}$ for the top and bottom detector, respectively. With these factors the measured change of position signal (V) is translated into a spot displacement (m), which we need for the calculation of the curvature signal.

With the two beam setup, we probe the change of slope, i.e., the curvature, between the two spots where the beams hit the crystal surface. The benefit of using two beams is that we have access to the curvature data directly. We can compare the displacement of the reflected beams on the two photodetectors. The same displacement indicates that the slope of the reflecting sample surface is the same for both spots, and this rules out curvature as the cause of the position signal change. Rather noise induced signal changes, such as tilting and vibrating of the manipulator and thermal drift, might cause such a signal change. Thus, by exploiting the curvature signal, the detrimental impact of noise- and thermally-induced sample and manipulator movements is greatly reduced. These aspects are important, as tiny laser beam movements on the nm scale on the split-photodetectors are readily sensed by the setup.

The link between the laser beam displacement on the top and bottom split-photodiodes, Δ_{top} , Δ_{bottom} , and the change

of curvature $\Delta\kappa$ is given by the geometry of the setup by

$$\Delta\kappa = \frac{\Delta_{\text{top}} - \Delta_{\text{bottom}}}{2l_{\text{spot}}l_{\text{PD}}}, \quad (1)$$

where l_{spot} and l_{PD} are the spot separation on the crystal surface ($\approx 4 \text{ mm}$) and the distance from the crystal surface to the detector ($\approx 250 \text{ mm}$), respectively.

The stress change $\Delta\tau_S$ is calculated as shown in Eq. (2) (Refs. 11, 19, and 33)

$$\Delta\tau_S = \frac{Yt_S^2}{6(1-\nu)}\Delta\kappa = \frac{Yt_S^2}{12(1-\nu)}\frac{\Delta_{\text{top}} - \Delta_{\text{bottom}}}{2l_{\text{spot}}l_{\text{PD}}}, \quad (2)$$

where the Young modulus Y and the Poisson ratio ν are calculated for the surface orientation of the sample;¹⁹ t_S is the thickness of the cantilever crystal. This so called modified Stoney equation relies on the assumption of a free two-dimensional bending, which is justified here in view of the large length-to-width ratio of the crystal and a curvature measurement at the free bottom end of the crystal.¹¹ Equation (2) is valid for isotropic stress. In case of anisotropic stress the crystal curvature needs to be measured along two orthogonal crystallographic directions.^{33,34}

The experimental determination of the spot separation l_{spot} , the detector-sample distance l_{PD} and the sample thickness t_S govern the accuracy of the measurement. The spot separation is measured by moving the sample manipulator vertically up, until the reflected intensity of the lower laser beam drops by a factor of two. Then, the distance travelled until the top beam suffers the same loss of reflected intensity gives the spot separation. We use an high precision manipulator³⁵ with micrometer dials for the travel, and this distance can be determined with an accuracy of order 0.1 mm . In view of the spot separation of order 4 mm , this amounts to a relative error of 2.5% . The experimental determinations of $l_{\text{PD}} \approx 250 \text{ mm}$ is performed with an accuracy of 1 mm , and this gives a relative error of $\pm 0.4\%$. The sample thickness t_S is measured by a thickness gauge,³⁶ and by determining the mass of the crystal and calculating the thickness from length, width, and density. These measurements require a careful manipulation of the delicate crystal. Alternatively, we also extract t_S from the resonance frequencies of flexural vibrations of the cantilevered crystal. This is done *in situ*, with the crystal mounted to the manipulator as shown in Fig. 1 above. Flexural vibrations of the crystal are excited by a loudspeaker placed on top of the manipulator. We monitor the vibration of the sample by measuring the AC component of the position signal as a function of the exciting frequency. The thickness of the sample is then determined from the resonance frequency f_i by the following equation:⁹

$$t_S = \frac{4\pi l_{\text{free}}^2}{\beta_i \sqrt{\frac{Y}{3\rho}}} f_i,$$

where ρ is the density and l_{free} is the free length of the cantilever crystal. The β_i are solutions of the equation $\cos \beta_i \cosh \beta_i + 1 = 0$. For the first 3 oscillation modes the values are $\beta_1 = 1.8751$, $\beta_2 = 4.6941$, and $\beta_3 = 7.8548$. With $l_{\text{free}} = 11 \pm 0.1 \text{ mm}$ as measured optically, the first resonance frequency is $f_1 = 414.8 \text{ Hz}$, which gives $t_S = 105 \pm 2 \mu\text{m}$.

This result is in agreement with the other methods described above.

We conclude that the overall relative error of the curvature measurement is given largely by the accuracy of the determination of the spot separation and of the sample-detector distance, and it amounts to $\approx 5\%$.

Finally, we want to comment on the temperature dependence of the elastic constants.³⁷ This effect is found to be negligible³⁸ over our temperature range in view of other sources of error. The temperature variation of the elastic constants of Pt is less than $\approx 1\%$ between 300 and 4 K.

C. MOKE setup

The measurement of the magneto-optical Kerr-effect is a powerful technique to study the magnetic properties of ferromagnetic films with sub-monolayer sensitivity.¹⁸ An experimental challenge is the application of sizable magnetic fields under UHV conditions. We use a C-yoke magnet⁴⁰ with a variable air gap, which is operated by a bipolar power supply that can deliver ± 60 A and a voltage of ± 45 V. The magnet is placed directly below the UHV chamber. The sample is lowered into a glass tube (a UHV-tight metal-glass-metal adapter⁴¹) by a long travel (600 mm) manipulator³⁵ between the pole pieces of the magnet as Fig. 4 (a) shows. The maximum field at the sample position is ± 0.7 T.

MOKE measurements can be performed in the in-plane (longitudinal MOKE or LMOKE) and in the out-of-plane geometry (polar MOKE or PMOKE). Figure 4(b) shows a simple way to switch between longitudinal and polar MOKE measurements by rotating the sample by 90° . Thus, in-plane and out-of-plane directions of magnetization can be investigated. Small silver covered glass mirrors⁴² are used to direct the MOKE laser light. We use a laser diode with beam shaping optics (wavelength 670 nm, 3 mW).²⁹ The light is polarized by a Glan-Thompson polarizer⁴³ to create p-polarized light, which is used for our measurements. The MOKE photodetector diodes⁴⁴ are covered by a bandpass filter⁴⁵ to reduce the influence of stray light.

MOKE measurements are performed with the analyzer rotated out of extinction by $\delta = 2^\circ$ ($\hat{=} 34.9$ mrad) and monitoring the photo detector signal while the magnetic field is swept. The Kerr rotation ϕ' is calculated by

$$\phi' = \frac{\delta}{4I_0}(\Delta I),$$

as described in the literature.⁴⁶ Here, ΔI is the signal change of the photo detector upon reversing the saturation magnetization, and I_0 is the average photo detector signal measured for opposite saturation directions. The magnetic field is measured by a Hall sensor³⁹ at the magnet yoke, see Fig. 4, during the field scan. The field at the sample position has been calibrated before against the field measured at the yoke. We find a hysteresis free linear relation between both field values.

III. RESULTS AND DISCUSSION

All experiments were performed in the UHV chamber at a base pressure of 1×10^{-10} mbar. The Pt(111) cantilever

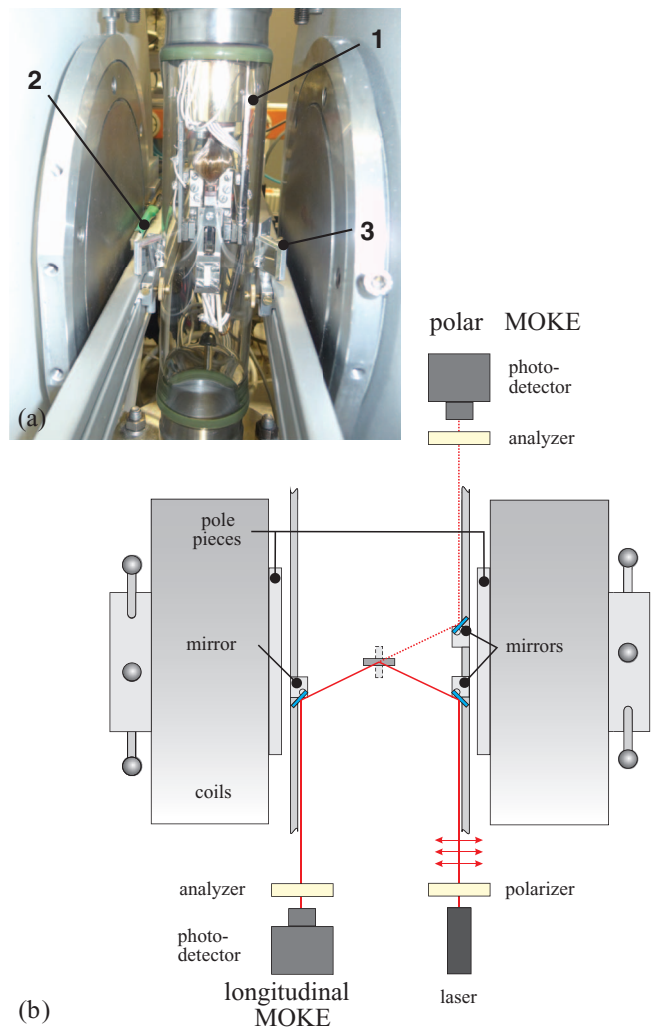


FIG. 4. (a) Front view of the lower part of the UHV system. The glass tube (1) of the UHV chamber is situated in the center between the yokes of the electromagnet (grey). 2: Hall probe,³⁹ 3: mirrors for deflecting the laser beam onto the sample; (b) Scheme of the setup for longitudinal and polar MOKE measurements. A rotation of the sample by 90° (dashed lines) allows measurements in polar geometry.

crystal was cleaned by sputtering with Ar^+ ions (beam energy 1.5 keV, sample current $1 \mu\text{A}$, 30 min), annealing in oxygen (5×10^{-7} mbar at 800 K for 30 s) and flashing to 1300 K for 5 s. The quality of the Pt(111) surface was checked by Auger electron spectroscopy and low energy electron diffraction. LEED shows a clear (1×1) diffraction pattern with low background intensity, and Auger electron spectroscopy reveals a clean surface where all contaminants have been removed to less than 1% surface coverage. The film thickness was checked by a calibrated quartz microbalance and determined with an accuracy of ± 0.2 ML.

In the following we present results on Co-induced stress on Pt(111), Xe-induced surface stress change on Pt(111), and on MOKE measurements for Co/Pt(111). Further experiments on systems which we studied before at 300 K at a different setup gave comparable results, and this indicates the functionality of our setup for low temperature and high magnetic field measurements.

A. Co-induced stress change

We are interested in the correlation between stress, strain, interface properties and magnetism of Co monolayers on Pt(111). Here, we present quantitative results on lattice stress and strain for the growth of Co on Pt(111) at 310 K, and of MOKE measurements. These data serve as a demonstration of the functionality of the setup, and an in-depth discussion is the topic of a future publication.

A considerable lattice mismatch of +10.7 % between Co and Pt results from the different in-plane atomic distances of both elements ($a_{\text{Pt}(111)} = 2.77 \text{ \AA}$, $a_{\text{Co},\text{fcc}(111)} = 2.51 \text{ \AA}$). A large lattice mismatch of this magnitude is expected to lead to considerable structural relaxation already in a few atomic layers thin films,¹⁹ and it is observed here.

Figure 5 shows the result of the stress measurement during the deposition of Co on Pt(111) at 310 K. The stress curve shows for a thickness below 2 ML a nonmonotonic change with increasing thickness, whereas above 2 ML a constant slope of the curve is observed up to the end of deposition at 5 ML. The slope of the curve in this thickness range corresponds to a film stress of +3.4 GPa.

A constant stress suggests a constant film strain between 2 and 5 ML. LEED shows distinct diffraction spots, indicative of an epitaxially ordered Co film. Figure 5 shows LEED images of the clean Pt(111) surface and of the 5 ML Co film on Pt(111). A quantitative analysis of the diffraction images reveals a different length of the reciprocal lattice vectors a_{Pt}^* and a_{Co}^* , which corresponds to an average Co film strain of +0.8%, significantly lower than the misfit strain of +10.7%. We apply continuum elasticity to calculate a film stress of +3.3 GPa from this lattice strain. This value is in good agree-

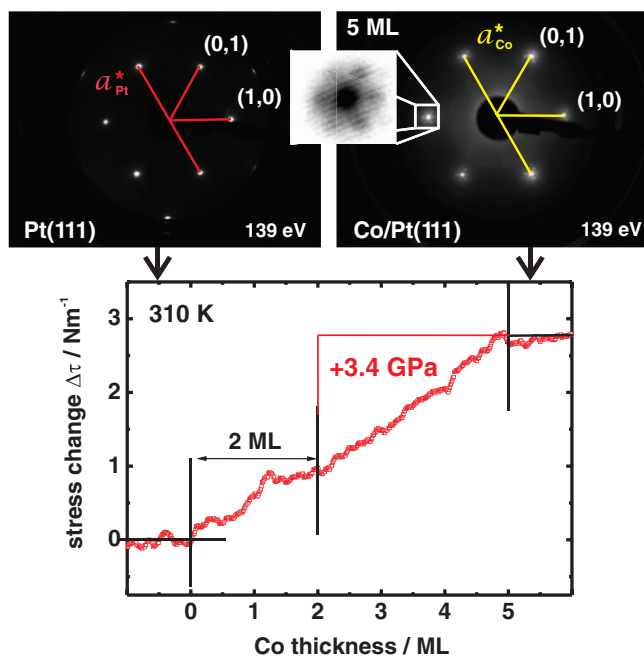


FIG. 5. Surface stress and LEED measurements during film growth of 5 ML Co on Pt(111) at 310 K. The red curve shows a tensile stress change, indicative of the residual strain in the film. The top row shows LEED images at 139 eV taken before and after film growth. The zoom-in (inverted) indicates satellite spots surrounding the central diffraction spot.

ment with the experimental result of +3.4 GPa. The observation of additional satellite diffraction spots in LEED is ascribed to a slight structural modulation⁴⁷ of the film, which involves spatially periodic shifts of Co atoms around an average film structure.

Our observation of a small Co-induced stress below 2 ML invalidates the assumption of a pseudomorphic Co film in the first layer. Rather, our observation provide evidence for a more complex growth mode at the Co-Pt interface, where the incorporation of Co into the Pt surface needs to be considered.⁴⁸

B. Surface stress change upon condensation of xenon

Low temperature measurements of adsorbate-induced surface stress change offer the possibility to study the impact of rare gas adsorption on surface stress. Corresponding measurements have not been performed yet, and this direction of research is still largely unexplored.

Figure 6 presents the Xe-induced surface stress change on Pt(111) upon condensation at 30 K. We measure an unexpected high compressive stress change of -2.2 N/m . We refer to the magnitude of surface stress change as unexpectedly large, as it equals the O-induced surface stress change on Pt(111) (-2.2 N/m).⁴⁹ There a strong chemical bond is acting, which is absent for physisorption of Xe. LEED images taken before and after Xe exposure at a partial pressure of 1×10^{-7} mbar for 320 s show the clean Pt surface and a

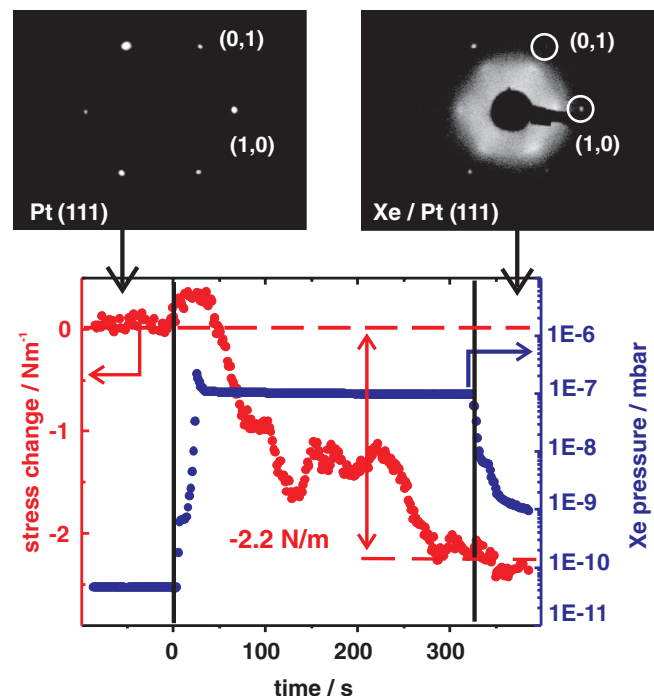


FIG. 6. Surface stress and LEED measurements during condensation of Xe on Pt(111) at 30 K. The red curve shows a compressive stress change upon exposure of the clean Pt(111) surface to Xe at a partial pressure (blue curve) of 1×10^{-7} mbar for 320 s. The top row LEED images are taken at 87 eV before and after Xe exposure. Upon Xe exposure an area of blurred diffracted intensity is found within the Pt first order diffraction peaks.

blurred Xe-induced superstructure, respectively. This LEED pattern suggests that Xe has condensed on the Pt(111) crystal, forming a not well ordered structure on top of the surface at 30 K. Slight annealing of this structure to 80 K induces the formation of an ordered Xe $\sqrt{3} \times \sqrt{3}$ surface structure.

A thorough understanding of the relation between rare gas condensation and surface stress change has not been achieved yet,^{50,51} and further experimental and theoretical investigations are called for to elucidate this largely unexplored topic.

C. Kerr effect measurements

We choose a thin-walled glass cylinder with an outer diameter of 51 mm and an inner diameter of 47 mm (Ref. 41) to provide an UHV access of the sample manipulator to the gap region of the electromagnet. High magnetic fields in combination with a light path which penetrates the glass cylinder surrounding the sample immediately lead to the question of the influence of Voigt and Faraday effects on the magneto-optical signal.⁵² The columns of Fig. 7 address these questions. They show the Kerr signals in longitudinal and polar geometries under different conditions during a magnetization loop with a maximum magnetic field of 0.7 T. Recently a MOKE setup

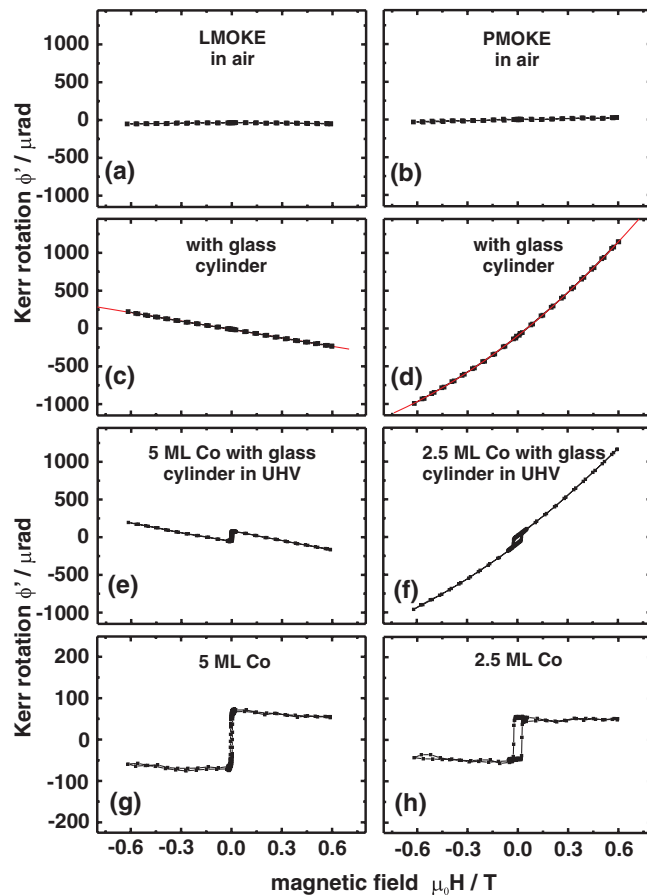


FIG. 7. Magneto-optical Kerr-effect measurements in longitudinal and polar geometry at 300 K. (a), (b) MOKE signal upon reflection from Pt(111), without glass cylinder. (c), (d) with glass cylinder. (e), (f) with Co monolayers and glass cylinder. (g), (h) from (e), (f) after background subtraction. For detailed explanations see text.

has been presented with all optical components within the UHV chamber. The contribution of magneto-optical signals from UHV windows can thus be avoided.⁵³ However, we refrain from this approach here, as we prefer to have direct access to the optical components of the MOKE experiment without breaking the vacuum.

The measurements (a), (b) were performed in air with a clean Pt crystal, where the glass cylinder was removed. (c) and (d) were taken under UHV conditions, where the glass cylinder was in the path of light. The fingerprint of the magneto-optical effects of the glass cylinder is apparent. In the longitudinal geometry we see the predominant influence of the Faraday effect, which is linear in field. In polar geometry a slight curvature indicates a contribution of the Voigt effect, which is quadratic in field. MOKE data on Co monolayers are shown in Figs. 7(e) and 7(f) for both geometries. The film thickness of 2.5 and 5 ML give easy axis hysteresis loops in longitudinal and in polar geometry, respectively. The curves reveal a sizable contribution of the glass cylinder to the MOKE signal measured of the Co monolayers at high fields.

To account for the signal contribution of the glass cylinder we subtract it (Figs. 7(c) and 7(d)) from the raw MOKE curves (Figs. 7(e) and 7(f)), and we obtain the MOKE curves presented in Figs. 7(g) and 7(h). Rectangular hysteresis curves with full remanence indicate easy axis magnetization loops.

Figure 8 shows longitudinal ((a),(c)) and polar ((b),(d)) measurements at 2.5 and 5 ML Co thickness. The same background subtraction method has been applied as described above. For 2.5 ML the MOKE curves show no appreciable signal change in LMOKE, but a clear hysteresis in PMOKE. This indicates an easy out-of-plane magnetization direction of the 2.5 ML film. LMOKE and PMOKE measurements of the 5 ML film reveal an easy in-plane magnetization direction, and an hard axis out-of-plane Kerr curve. The maximum field of 0.7 T is just sufficient to saturate the signal in the hard out-of-plane magnetization direction. This allows us to extract the effective magnetic anisotropy of this film⁵⁴ from its spontaneous magnetization $M_s = 1447$ kA/m and its anisotropy

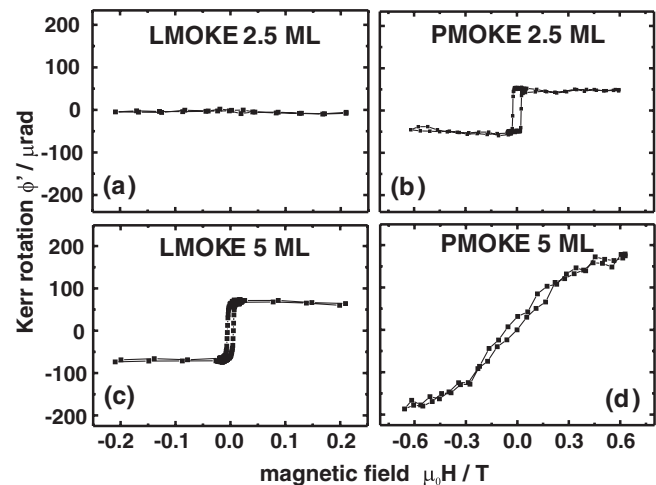


FIG. 8. MOKE of Co films with a thickness of 2.5 ML (a),(b) and 5 ML (c),(d) on Pt(111) in longitudinal and polar geometry, respectively. The 2.5 ML Co film shows an easy out-of-plane axis of magnetization, whereas it is in-plane for 5 ML. Faraday and Voigt effects have been subtracted.

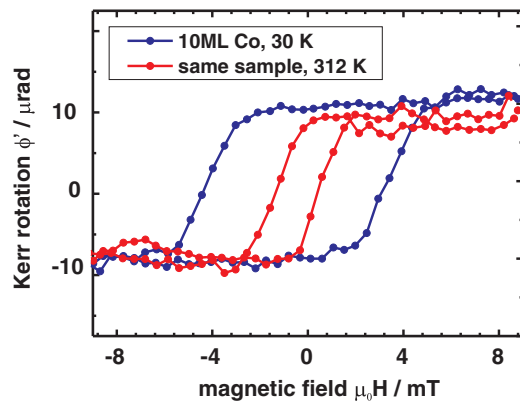


FIG. 9. Longitudinal MOKE measurement of 10 ML Co/Pt(111). The red curve shows the MOKE signal at 312 K, the blue at 30 K. No background subtraction has been performed.

field H_{an} of 0.7 T as $K_{eff} = 0.5\mu_0 M_s H_{an} = 0.51 \text{ MJ/m}^3$. The anisotropy of the 2.5 ML film is apparently larger, and no significant MOKE sign change is observed for magnetization along the hard in-plane direction.

We complete the presentation of MOKE results with measurements of a 10 ML Co film performed at 312 K (red curve) and 30 K (blue curve) in Fig. 9. Here, the moderate field below 10 mT leads to negligible contributions of Faraday and Voigt effects of the glass cylinder, and a background correction as described above has not been performed. The increase of the coercivity by a factor of almost 4 at low temperature is striking. It indicates that magnetization reversal is a thermally activated process, and it leads in general to an increase of coercivity with decreasing temperature.⁵⁵

IV. CONCLUSIONS

We have developed a liquid helium cooled stress measurement setup which uses an optical 2-beam cantilever technique. It extends the accessible temperature range down to 30 K. It combines stress measurements with magneto-optical Kerr-effect measurements at low temperatures and in high magnetic fields of up to 0.7 T. First measurements indicate the functionality of the setup. It opens new venues for the characterization of magnetic and adsorbate-induced effects at low temperatures. Applications are foreseen in the field of condensation of rare gases on metal surfaces and for the studies of the magnetic properties of magnetic monolayers and nanostructures. The experimental setup is currently enhanced to include pulsed laser deposition. Thus, the *in situ* investigation of stress and magnetism of oxides and multiferroic compounds will be possible.

ACKNOWLEDGMENTS

Partial support by SFB 762 is gratefully acknowledged.

- ¹V. Buck, *Z. Phys. B: Condens. Matter* **33**, 349 (1979).
²R. Koch and R. Abermann, *Thin Solid Films* **129**, 63 (1985).
³A. J. Schell-Sorokin and R. M. Tromp, *Phys. Rev. Lett.* **64**, 1039 (1990).

- ⁴R. E. Martinez, W. M. Augustyniak, and J. A. Golovchenko, *Phys. Rev. Lett.* **64**, 1035 (1990).
⁵R. Abermann, in *Selected Proceedings of the 11th International Vacuum Congress and 7th International Conference on Solid Surfaces* [Vacuum **41**, 1279 (1990)].
⁶M. Weber, R. Koch, and K. H. Rieder, *Phys. Rev. Lett.* **73**, 1166 (1994).
⁷P. Müller and R. Kern, *Surf. Sci.* **301**, 386 (1994).
⁸D. Sander, A. Enders, and J. Kirschner, *Rev. Sci. Instrum.* **66**, 4734 (1995).
⁹T. Gutjahr-Löser, "Magnetoelastische Kopplung in oligatomaren Filmen," Ph.D. dissertation (Martin-Luther-Universität, Halle-Wittenberg, 1999).
¹⁰F. Spaepen, *Acta Mater.* **48**, 31 (2000).
¹¹K. Dahmen, S. Lehwald, and H. Ibach, *Surf. Sci.* **446**, 161 (2000).
¹²K. Dahmen, H. Ibach, and D. Sander, *J. Magn. Magn. Mater.* **231**, 74 (2001).
¹³D. Sander, and H. Ibach, in *Landolt-Börnstein: Numerical Data and Functional Relationships in Science and Technology*, New Series III, Vol. 42, edited by H. P. Bonzel (Springer, Berlin, 2001) pp. 1–49.
¹⁴D. Sander, *Curr. Opin. Solid State Mater. Sci.* **7**, 51 (2003).
¹⁵D. Sander, H. Meyerheim, S. Ferrer, and J. Kirschner, in *Advances in Solid State Physics*, edited by B. Kramer (Springer, 2003), Vol. 43, pp. 547–561.
¹⁶P. Kury, T. Grabosch, and M. H. von Hoegen, *Rev. Sci. Instrum.* **76**, 023903 (2005).
¹⁷D. Sander, Z. Tian, and J. Kirschner, *Sensors* **8**, 4466 (2008).
¹⁸S. Bader, *J. Magn. Magn. Mater.* **100**, 440 (1991).
¹⁹D. Sander, *Rep. Prog. Phys.* **62**, 809 (1999).
²⁰S. Ouazi, S. Wedekind, G. Rodary, H. Oka, D. Sander, and J. Kirschner, *Phys. Rev. Lett.* **108**, 107206 (2012).
²¹J. Juraszek, O. Zivotsky, H. Chiron, C. Vaudolon, and J. Teillet, *Rev. Sci. Instrum.* **80**, 043905 (2009).
²²M. Gilbert, H.-C. Mertins, M. Tesch, O. Berges, H. Feilbach, and C. M. Schneider, *Rev. Sci. Instrum.* **83**, 025109 (2012).
²³A. Arora, S. Ghosh, and V. Sugunakar, *Rev. Sci. Instrum.* **82**, 123903 (2011).
²⁴CryoVac Gesellschaft für Tieftemperaturtechnik mbH & Co KG, Heuserweg 14, 53842 Troisdorf, Germany, see <http://www.CryoVac.de>.
²⁵MaTeck GmbH, Im Langenbroich 20, D-52428 Juelich, see <http://www.mateck.de>.
²⁶LakeShore, Temperature Measurement and Control Catalog, see <http://www.lakeshore.com>.
²⁷Mikro-Pyrometer PB 06, KELLER HCW GmbH Division MSR, Carl-Keller-Strasse 2-10, D-49479 Ibbenbüren-Laggenbeck, see <http://www.keller-msr.de>.
²⁸IMPAC-Pyrometer IGA 140 with wavelength 1.45-1.8 micrometer, 300 °C-1300 °C, LumaSense Technologies GmbH, Kleyerstr. 90, D-60326 Frankfurt/Main, see www.lumasenseinc.com.
²⁹5MM - 325-0,8 +25CM - 670-3 -TO7 - A4.5-2, Schäfter+Kirchhoff GmbH, Kieler Straße 212, 22525 Hamburg, see <http://www.SuKHamburg.de>.
³⁰Segmented Photodiode, SPOT Series SPOT-2DMI TO-18, through OSI Optoelectronics, see <http://www.osioptoelectronics.com>.
³¹Model 301-DIV (2×), UDT Instruments, San Diego, CA, see <http://www.udtinstruments.com>.
³²P-841.10 with E-665 LVPZT Controller/Amplifier, PI, Physik Instrumente GmbH & Co. KG; Römerstraße 1, 76228 Karlsruhe, Germany, see <http://www.pi.ws>.
³³H. Ibach, *Surf. Sci. Rep.* **29**, 195 (1997).
³⁴D. Sander, A. Enders, and J. Kirschner, *Europhys. Lett.* **45**, 208 (1999).
³⁵Omniax Translator with a z-travel of 600 mm, VG Scienta Ltd, Maunsell Road, Hastings, TN38 9NN, UK, see <http://www.vgsienta.com>.
³⁶Mitutoyo thickness gauge 543-250B, range 12.7mm, resolution 0.001 mm, Mitutoyo Deutschland GmbH, Borsigstr. 8-10, 41469 Neuss, see <http://www2.mitutoyo.de>.
³⁷P. Kury and M. H. von Hoegen, *Rev. Sci. Instrum.* **75**, 1357 (2004).
³⁸R. F. S. Hearmon, in *Landolt Boernstein-Numerical Data*, edited by K.-H. Hellwege, and A. M. Hellwege (Springer, 1969), Vol. 3, pp. 1–19.
³⁹DTM-151 Digital Teslameter and MPT-141 Hall Probe, Group3-Technology, 2 Charann Place, Avondale, Auckland 1026, New Zealand, see <http://www.group3technology.com>.
⁴⁰Magnet B-E 15, B-MN 45/60, B-MC 1, Bruker Corporation, see <http://www.bruker.com>.
⁴¹Metal-glass-metal adapter SPS-200-T-GL 186 mm including 2× NW63CF flange, Hositrad Vacuum Technology, Lindnergasse 2, 093047 Regensburg, Germany, see <http://www.hositrad.com>.

- ⁴²Silver coated plane glass mirrors, G340331400, RAGV, bxL=10×15, d=2; L/10, Qioptiq Photonics GmbH & Co. KG, Königsallee 23, 37081 Göttingen, Germany, see <http://www.qioptiq.de>.
- ⁴³Extinction ratio 0.000001, Bernhard Halle Nachfolger GmbH, Hubertusstraße 10, D - 12163 Berlin, see <http://www.b-halle.de>.
- ⁴⁴Planar Diffused Silicon Photodiode PIN-6DI TO-8, through OSI Optoelectronics, see <http://www.osioptoelectronics.com>.
- ⁴⁵03Fil054 670 nm laser filter, MellesGriot GmbH, Lilienthalstraße 30-32, 64625 Bensheim, Germany, see <http://www.cvimellesgriot.com>.
- ⁴⁶Z. Q. Qiu and S. D. Bader, *J. Magn. Magn. Mater.* **200**, 664 (1999).
- ⁴⁷R. Popescu, H. L. Meyerheim, D. Sander, J. Kirschner, P. Steadman, O. Robach, and S. Ferrer, *Phys. Rev. B* **68**, 155421 (2003).
- ⁴⁸P. Varga, E. Lundgren, J. Redinger, and M. Schmid, *Phys. Status Solidi A* **187**, 97 (2001).
- ⁴⁹Z. Tian, D. Sander, N. N. Negulyaev, V. S. Stepanyuk, and J. Kirschner, *Phys. Rev. B* **81**, 113407 (2010).
- ⁵⁰J. E. Müller, *Phys. Rev. Lett.* **65**, 3021 (1990).
- ⁵¹J. L. F. D. Silva, C. Stampfl, and M. Scheffler, *Phys. Rev. Lett.* **90**, 066104 (2003).
- ⁵²M. Freiser, *IEEE Trans. Magn.* **4**, 152 (1968).
- ⁵³A. Lehnert, P. Bulushek, N. Weiss, J. Giesecke, M. Treier, S. Rusponi, and H. Brune, *Rev. Sci. Instrum.* **80**, 023902 (2009).
- ⁵⁴D. Sander, *J. Phys.: Condens. Matter* **16**, R603 (2004).
- ⁵⁵E. Kneller, *Ferromagnetismus* (Springer, 1962).